JOINT CENTER FOR SATELLITE DATA ASSIMILATION

NO. 59, SPRING 2018

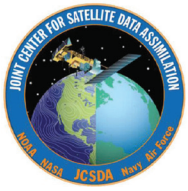

JCSDA Quarterly

NOAA | NASA | US NAVY | US AIR FORCE

https://doi.org/10.7289/V5/Q-JCSDA-59-2018

NEWS IN THIS QUARTER

SCIENCE UPDATE

Using Multi-Sensor Aerosol Optical Depth Retrievals to Improve Infrared Radiance Assimilation

Space-borne satellite sensors measure varying aerosol mass concentrations and particle sizes throughout the globe (e.g., Remer et al., 2008). For dust aerosols in particular, the coarse particles are capable of scattering and absorbing both solar and infrared radiation, which can lead to considerable warming and cooling effects at these longer wavelengths (e.g., Zhang and Christopher, 2003). Naeger et al. (2013a) found long wave (LW) heating rates of greater than 1 K d^{-1} within a Saharan dust layer composed of particles larger than 2 µm in radius, along with cooling rates of greater than 1.5 K d^{-1} near the top of the layer. Comparable LW heating and cooling rates were found for dust storms over the Taklimakan desert in northern China (Huang et al., 2009), which showed further evidence that coarse dust particles can significantly impact infrared radiances measured by satellite sensors.

Infrared radiances in clear-sky conditions are regularly assimilated into numerical weather prediction (NWP) systems at operational centers to provide more realistic initial conditions for forecast models. Data assimilation (DA) systems are composed of a forward radiative transfer model, which simulates the observed satellite radiances at specific wavelengths from a given model background or atmospheric state. The exclusion of cloud-affected radiances limit the number of observations provided to the DA systems, since global average cloud coverage is greater than 70% (Wylie et al., 2005). Furthermore, aerosols such as coarse mode dust particles may impact the clear-sky satellite radiances, which can introduce significant biases in temperature, moisture, and wind analysis fields of a model, and consequently, reduce the forecast skill (Wang and Niu, 2013). The objective of this project is to improve the assimilation of aerosol-affected radiances into NWP models (i.e., global Goddard Earth

(continued on page 2)

IN THIS ISSUE

Observing System Model Version 5 (GEOS-5) system) within the Gridpoint Statistical Interpolation (GSI) by reducing the forward model error through incorporation of a robust aerosol optical depth (AOD) product (Naeger et al., 2016) into the Community Radiative Transfer Model (CRTM).

Prior to assimilating aerosol-affected radiances into the GEOS-5 framework, we diagnose the ability of the CRTM to simulate dust aerosol-affected infrared radiances. Our careful validation work utilizes space-based Cloud Aerosol LIdar with Orthogonal Polarization (CALIOP) measurements along with ground-based AErosol RObotic NETwork (AERONET) aerosol retrievals to provide detailed aerosol profiles for input into the CRTM. Calculated aerosol-corrected satellite radiances are compared to uncorrected radiances from the CRTM and evaluated against infrared radiance observations. This report presents results from the CRTM validation component of this project.

A large dust storm originated from the Gobi Desert in eastern Asia during the passage of a low-pressure system. Strong low-level winds efficiently transported the dust over the Sea of Japan and the western Pacific, which allowed for the coarse particles to significantly impact infrared radiances over a large region. This particular dust episode was ideal for the CRTM validation work, since it was well observed by space-based and ground-based instruments. The Advanced Himawari Imager (AHI) onboard Himwari-8 observed the dust plume over eastern China on 4 May 2017. The AHI scan at 0510 UTC is of particular interest for this work, since the CALIOP transected over the dust plume at this time. The AHI red-green-blue (RGB) dust image highlights dusty regions primarily through the input to the R component, which is the difference between the 12.4 μm – 11.2 μm channels, as absorbing coarse mode dust particles generally absorb more radiation at 11.2 μm compared to 12.4 μm. As a result, dust particles can influence positive difference between these channels depending on the optical thickness and height of the plume, which leads to a greater contribution from R component in the RGB image. The brighter pink colors in the AHI RGB image on 4 May 2017 (Figure 1a) indicate that an optically thick dust plume composed of coarse mode particles trailed behind a cloud band over eastern China.

The CALIOP measured enhanced 532 nm attenuated backscatter between 1 and 4 km in height from about 41° to 45°N along the transect (Figure 1b). The vertical feature mask (VFM) from CALIOP identified this area of enhanced backscatter as dust aerosols, while highly backscattering clouds were identified to the south and north of the dusty region. Columnar AOD retrievals from CALIOP within the dust region were between 1.5 and 2.5 (not shown), which were in general agreement with "gold standard" AERONET AOD retrievals at Beijing (black circle in Figure 1a) where values were around 2.0 (Figure 1c). This quantitative agreement between AERONET and CALIOP AOD provided confidence that vertical profile retrievals from CALIOP within the dust plume were suitable for input in the CRTM. We converted 532 nm AOD profiles from CALIOP to mass concentrations using Equation (1)

$$M^{type,size} = \frac{1.33 * \rho * AOD * r_e}{Q^{type,size}} \quad (1),$$

(continued on page 3)

JOINT CENTER FOR SATELLITE DATA ASSIMILATION

5830 University Research Court
College Park, Maryland 20740

Website: www.jcsda.noaa.gov

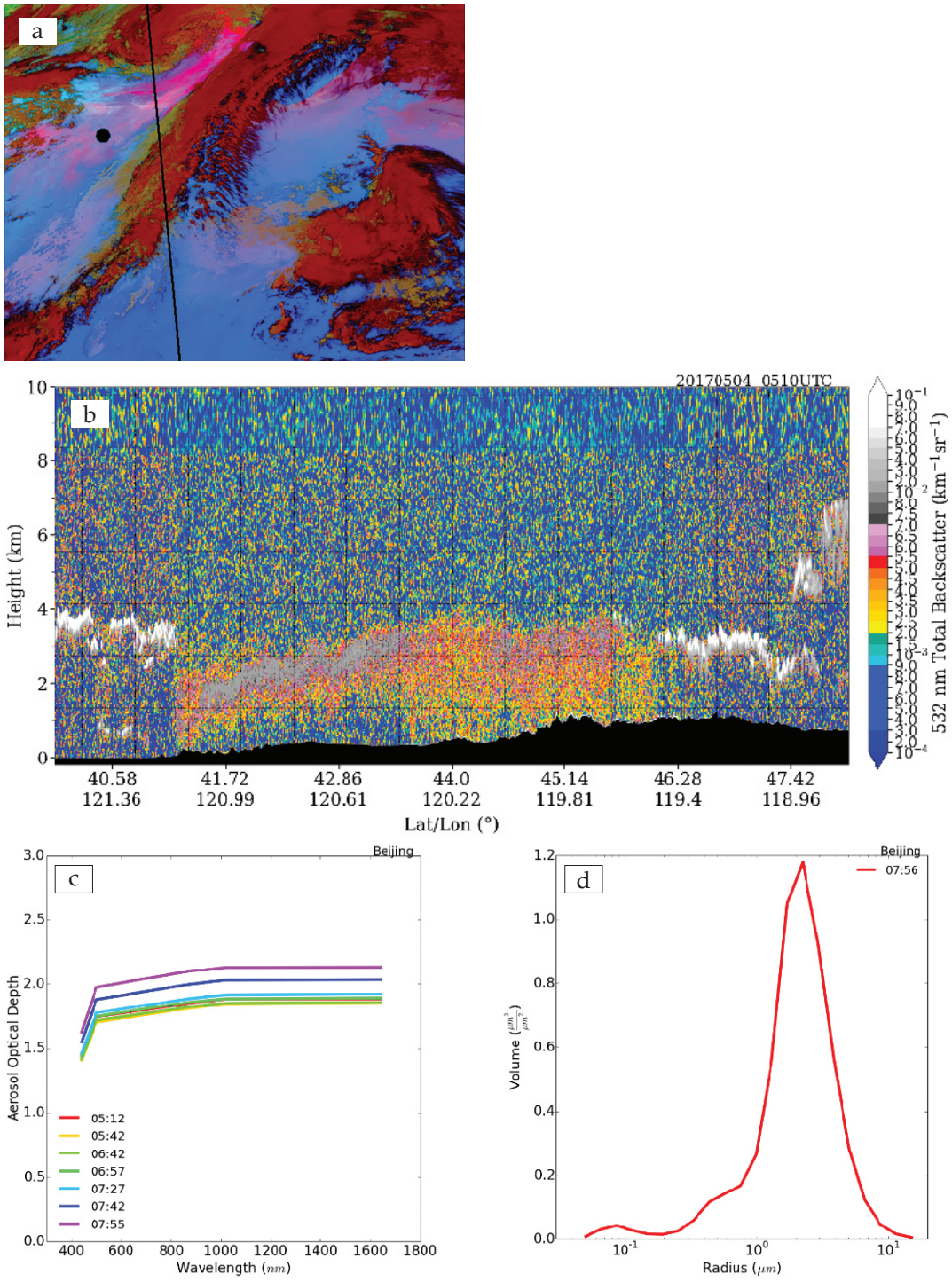

Figure 1. *(a) AHI dust RGB image at 0510 UTC on 4 May 2017 with CALIOP transect highlighted by the black line and the AERONET site at Beijing shown by the black circle. The dust RGB uses the 12.4 - 11.2 μm band difference for the R component, 11.2 – 8.6 μm band difference for the G component, and the 11.2 μm band for the B component. (b) CALIOP 532 nm attenuated backscatter measurements along portion of transect in (a). (c,d) AERONET AOD and size distribution retrievals at the Beijing site from 05 to 08 UTC on 4 May.*

where ρ is the particle density, r_e is the effective radius, and Q is the extinction coefficient. For solving equation (1), we assumed a ρ of 2.6 g cm^{-3} for all dust aerosol sizes for consistency with the Goddard Chemistry Aerosol Radiation and Transport (GOCART) model used in the CRTM aerosol module, which prescribes identical ρ values for the 5 dust bin sizes. Refractive indices and mean radius from AERONET were used as input into Mie-scattering code for

(continued on page 4)

calculating a realistic Q, which is consistent with the spherical particle assumption in the CRTM aerosol module. Imaginary refractive indices of about 0.003 at 440 nm from AERONET were quite typical for dust aerosols (not shown), while the particle size distribution from AERONET showed a strong peak in the coarse mode of around 2 µm radius and a minimal peak in the fine mode (Figure 1d). After gathering the necessary parameters from AERONET and CALIOP retrievals for Equation (1), we calculated dust mass concentration profiles for input into the CRTM. For the meteorological input profiles into the CRTM, we used Modern-Era Retrospective analysis for Research and Applications, Version 2 (MERRA-2) data with a horizontal resolution of 0.5°x0.625° in the latitude and longitude, respectively, and 72 hybrid-eta levels from the surface to 0.01 hPa. We conducted two separate CRTM experiments for each case study, one with only meteorology input (neglect aerosols; aerosol-free experiment) and one with meteorology and aerosol inputs (dusty experiment). The CRTM output of simulated infrared radiances and brightness temperatures were compared to those observed from the MODIS and AHI satellite sensors. This report focuses on the simulated versus observed satellite radiances from the AHI bands 11 (8.6 µm), 13 (10.4 µm), 14 (11.2 µm), and 15 (12.4 µm). These bands are of particular interest due to the known scattering and absorbing effects of dust aerosols at these wavelengths.

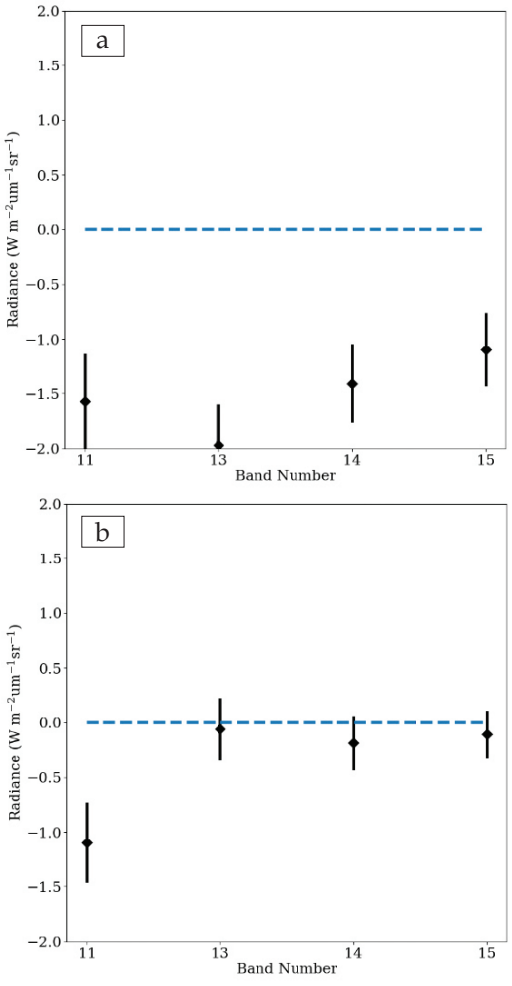

Figure 2. *(a) Mean difference between the observed and simulated AHI radiances at band 11 (8.6 µm), 13 (10.4 µm), 14 (11.2 µm), and 15 (12.4 µm) for the aerosol-free CRTM experiment. (b) Same as (a), except for the dusty CRTM experiment. The vertical black lines represent the standard deviation at each band.*

Our CRTM results highlight the large impacts on the AHI infrared radiances from the dust plume on 4 May 2017. When assuming an aerosol-free atmosphere, the CRTM simulated radiances are significantly higher for all the AHI bands, particularly at 10.4 µm where simulated radiances are higher than observations by about 2 W m^{-2} µm^{-1} sr^{-1} (Figure 2a). When accounting for aerosols in the CRTM, the simulated radiances are significantly reduced due to the absorption characteristics of the dust particles, which result in an overall much better comparison between the simulated and observed radiances (Figure 2b). The most drastic improvement occurs in the 10.4 µm band as simulated radiances are only slightly overestimated when accounting for aerosols in the CRTM, which indicates the strong sensitivity to the absorption characteristics of dust aerosols at this wavelength. Although substantial improvements in the simulated

(continued on page 5)

radiances are also shown in the 11.2 and 12.4 μm bands, the stronger water vapor absorption at these wavelengths leads to a reduction in the radiance differences between the aerosol-free and dusty experiments. Also, the weaker dust absorption characteristics at 12.4 μm further reduces the radiance differences at this wavelength compared to 11.2 μm. Much less improvement is shown in the 8.6 μm band, which is likely tied to the fact that this wavelength is more sensitive to the dust composition than the larger infrared wavelengths (Sokolik, 2002). Thus, the prescribed dust optical properties in the CRTM lookup tables based on the GOCART model are misrepresentative of the actual properties of the dust plume. For this case, the prescribed aerosol extinction coefficients are likely underestimated around 8.6 μm, which is leading to the overestimation in the simulated AHI radiances at this wavelength. It is also important to note that standard deviation of the observed versus simulated radiance differences is lower for the dusty experiment, since the presence of dust masks some of the surface emissivity and temperature effects on the top-of-atmosphere infrared radiances. The larger standard deviation at 8.6 μm compared to the other bands are further indicative of the strong sensitivity to the dust composition and the overall larger uncertainties with the CRTM simulated infrared radiances at this wavelength.

The dust storm on 4 May 2017 continued its eastward transport to over the Sea of Japan where the CALIOP captured the plume several days later on 7 May. The dust was also observed at the nearby AERONET Hokkaido site in Japan. The AHI dust RGB image shows some brighter pink colors over the Sea of Japan associated with the dust plume, albeit the pink colors are not nearly as bright as the optically thick dust plume on 4 May (Figure 3a). CALIOP measurements reveal light to moderate backscatter from near the surface to approximately 2.5 km in height along the transect with the largest backscatter occurring from about 40° to 42°N (Figure 3b). AERONET AOD retrievals struggle to reach 0.3 for this long-range transported dust plume (Figure 3c), but cloud cover over the Hokkaido site likely hindered the instrument from measuring the more intense portions of the plume. Conversely, CALIOP AOD exceeds 1 in the areas of largest backscatter along the transect, which adequately compares to MODIS Aqua AOD retrievals (not shown). Nevertheless, the AERONET size distribution measurements were still applicable for this dust plume as the distribution is dominated by coarse particles with a peak near 3 μm; however, the coarse mode distribution is much broader for this long-range transported case compared to the rather narrow coarse mode observed over Beijing on 4 May. We use the same methodology as discussed for the previous case to run aerosol-free and dusty CRTM experiments and compare the simulated and observed AHI infrared radiances.

Similar to the previous case, the dusty CRTM experiments lead to an overall improvement in the simulated AHI radiances at 10.4, 11.2, and 12.4 μm (Figure 4). Once again, the dust particles have the largest impact in the 10.4 μm band, which leads to a very close agreement between the simulated and observed radiances at this wavelength. The dusty CRTM experiments lead to only minimal improvement in the 8.6 μm band, which further suggests that the dust extinction coefficients around 8.6 μm in the

(continued on page 6)

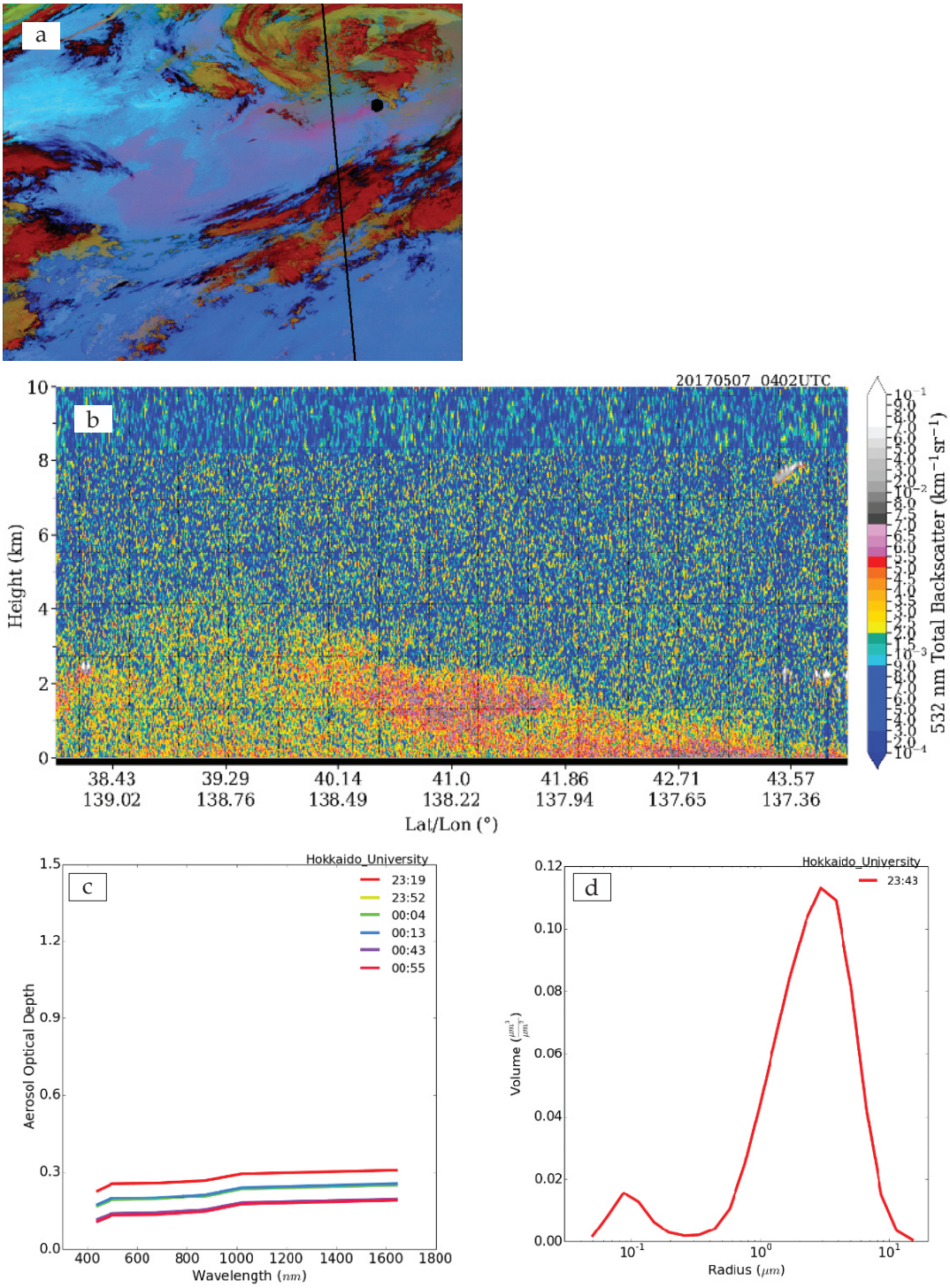

Figure 3. *Similar panels as Figure 1, except for the long-range transported dust case on 7 May 2017. (a) AHI dust image is valid at 0410 UTC and AERONET site at Hokkaido is indicated by black circle. (b) CALIOP 532 nm attenuated backscatter measurements along portion of transect in (a). (c,d) AERONET retrievals from 2300 UTC 6 May to 01 UTC 7 May at Hokkaido are shown.*

CRTM lookup table may not be applicable for dust emitted from the Gobi desert. There is a much weaker impact of dust on the infrared AHI radiances compared to the 4 May case, since the dust plume was optically thinner and located lower in the atmosphere for this case. Also, the dust impact on the infrared radiances was further limited by the fact that the low-level dust plume was over a cooler water surface on 7 May.

(continued on page 7)

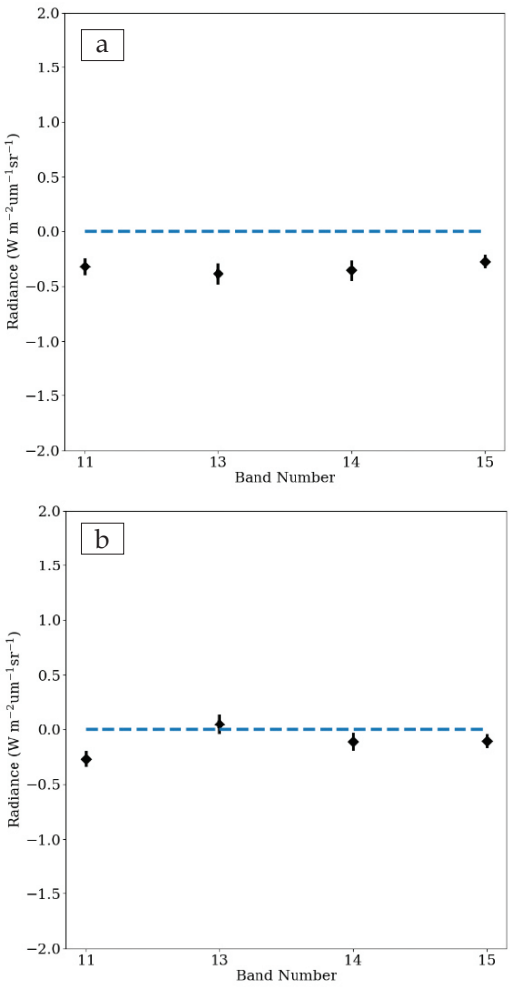

Figure 4. *Similar to panels in Figure 2, except for 7 May case.*

The results from this CRTM validation work indicate that the assimilation of aerosol-affected infrared radiances at 10.4, 11.2, and 12.4 μm could lead to significantly positive impacts on the forecast skill. At the current time, we find limited use for the 8.6 μm band due to the strong sensitivity to the dust composition, but adopting regionally prescribed dust optical properties may help promote the use of this band in the future. This project is currently investigating the impact of aerosol-affected infrared radiance assimilation using the GEOS-5 framework.

Aaron Naeger, University of Alabama in Huntsville, Earth System Science Center, aaron.naeger@nasa.gov

References

Huang, J., Q. Fu, J. Su, Q. Tang, P. Minnis, Y. Hu, Y. Yi, and Q. Zhao, 2009: Taklimakan dust aerosol radiative heating derived from CALIPSO observations using the Fu-Liou radiation model with CERES constraints. *Atmos. Chem. Phys.*, 9, 4011-4021, doi:10.5194/acp-9-4011-2009.

Naeger, A. R., P. Gupta, B. Zavodsky, and K. M. McGrath, 2016: Monitoring and tracking the trans-Pacific transport of aerosols using multi-satellite aerosol optical depth composites. *Atmos. Meas. Tech.*, 9, 2463-2482, doi:10.5194/amt-9-2463-2016.

Naeger, A. R., S. A. Christopher, and B. T. Johnson, 2013: Multiplatform analysis of the radiative effects and heating rates for an intense dust storm on 21 June 2007. *J. Geophys. Res. Atmos.*, 118, 9316–9329, doi:10.1002/jgrd.50713.

Remer, L. A., et al., 2008: Global aerosol climatology from the MODIS satellite sensors. *J. Geophys. Res.*, 113, D14S07, doi:10.1029/2007JD009661.

Sokolik, I. N., 2002: The spectral radiative signature of wind-blown mineral dust: Implications for remote sensing in the thermal IR region. *Geophys. Res. Lett.*, 29(24), 2154, doi:10.1029/2002GL015910.

Wang, H., and T. Niu, 2013: Sensitivity studies of aerosol data assimilation and direct radiative feedbacks in modeling dust aerosols. *Atmos. Environ.*, 64, 208–218.

Wylie, D., D. L. Jackson, W. P. Menzel, and J. J. Bates, 2005: Trends in global cloud cover in two decades of HIRS observations. *J. Clim.*, **18**(15), 3021–3031.

Zhang, J., and S. A. Christopher, 2003: Longwave radiative forcing of Saharan dust aerosols estimated from MODIS, MISR, and CERES observations on Terra. *Geophys. Res. Lett.*, 30, 2188, doi:10.1029/2003GL018479.

Improving scattering, absorption, polarization properties of snow, graupel, and ice aggregate particles from solar to microwave wavelengths in support of the CRTM

Introduction

The Community Radiative Transfer Model (CRTM) developed as a flagship product of the Joint Center for Satellite Data Assimilation (JCSDA) facilitates the incorporation of the multiple scattering effect associated with atmospheric particles into both forward models and inverse algorithms. This is essential for inferring cloud properties from radiances measured by satellite sensors. In addition to various types of aerosols, the CRTM also includes the optical properties of hydrometeors. It is computationally costly to compute the single-scattering properties if the computational capability is built in retrieval algorithms. For this reason, in practice the single-scattering property data sets are provided in the form of look up tables (LUTs) in the terms of coefficient files incorporated in the CRTM. The CRTM hydrometeor classes in ice phase are listed in Table 1.

A model design choice reflected in Table 1 is the fact that the CRTM does not consider a continuous spectrum of hydrometeor morphologies and densities. Instead, it uses four hydrometeor types defined by McCumber et al. (1991). The scattering of shortwave solar, longwave infrared (IR), and microwave (MW) radiation is incorporated in the CRTM, particularly both radiative transfer solvers currently implemented in the CRTM, namely the so-called Advanced Doubling-Adding Method (ADA) by Liu et al. (2006) and the Successive-Order-of-Interaction Radiative Transfer Model by Heidinger et al. (2006) with the ADA as the default solver.

Category	Density [g/cm^3]
Cloud ice	0.900
Graupel & Hail	0.400
Snow	0.100

Table 1. *Solid Hydrometeor Categories and associated densities in the CRTM Release 2.1.3*

Single-Scattering Properties

As the existing CRTM hydrometeor scattering coefficients are based on the Lorenz-Mie theory for spherical particles, a straightforward idea to enhance the accuracy of the CRTM is to incorporate the

(continued on page 9)

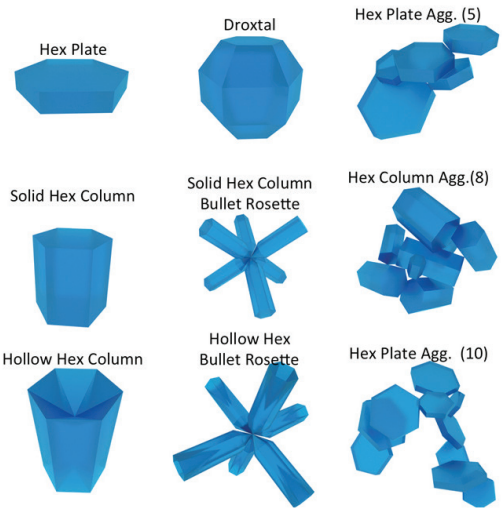

Figure 1. *Various ice crystal shapes/habits defined for light scattering calculation.*

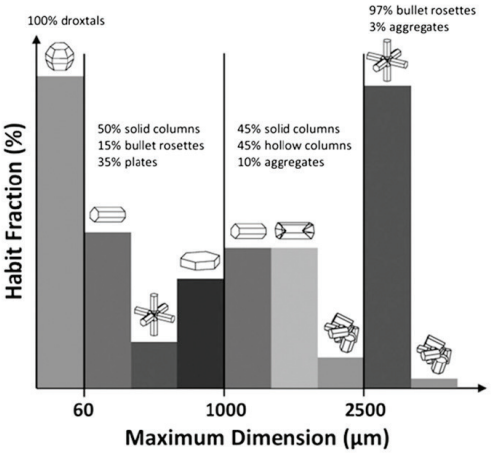

Figure 2. *MODIS Collection 5 (MC5) ice crystal habit fraction vs. size (Baum et al., 2005)*

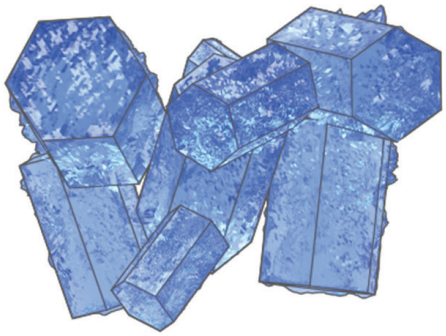

Figure 3. *MODIS Collection 6 (MC6) single habit roughened column aggregate ice particle model.*

recent advances in the discipline of light scattering research. Numerous numerical and analytical techniques have been developed and refined over the last decades to compute the light scattering properties of highly- complex particles, such as the ones listed in Table 1. Advanced light-scattering computational techniques include the Invariant-Imbedding T-Matrix (IITM) method (Bi and Yang, 2014 and references cited therein), the Improved Geometrical Optics Method (IGOM); (Yang and Liou, 1996a), and the Finite Difference Time Domain (FDTD) approach (Yee, 1966; Yang and Liou, 1996b). In the past, these methods have been used to compute the Moderate Resolution Imaging Spectroradiometer (MODIS) Collection 5 and 6 (MC5 & MC6) ice cloud single-scattering properties used in the MODIS operational retrievals (Baum et al. 2005; Platnick et al., 2017).

Figure 1 shows various types of ice crystal shapes/habits defined for light scattering computation. A mixture of six ice crystal habits for the MC5 cloud property retrievals is shown in Fig. 2 (Baum et al., 2005). In contrast, the MC6 model consists of a single habit shown in Fig. 3 (Platnick et al. 2017). This particle model consists of an aggregate of severely roughened hexagonal columns.

The single-scattering properties of the ice hydrometeor class in Table 1 have been updated using the MC6 ice cloud optical properties by incorporating the temperature dependence of the refractive index of water ice (Iwabuchi and Yang, 2011). The imaginary part of the refractive index of ice is shown in Fig. 4.

The effect of the temperature dependence on the bulk phase matrix of MC6 ice cloud model for particles with an effective radius of 800 μm at frequencies 10.7 and 89 GHz and at temperatures 160 and 230 K (Yi et al., 2016) is shown in Fig. 5. The results of a canonical case for Atmospheric Infrared

(continued on page 10)

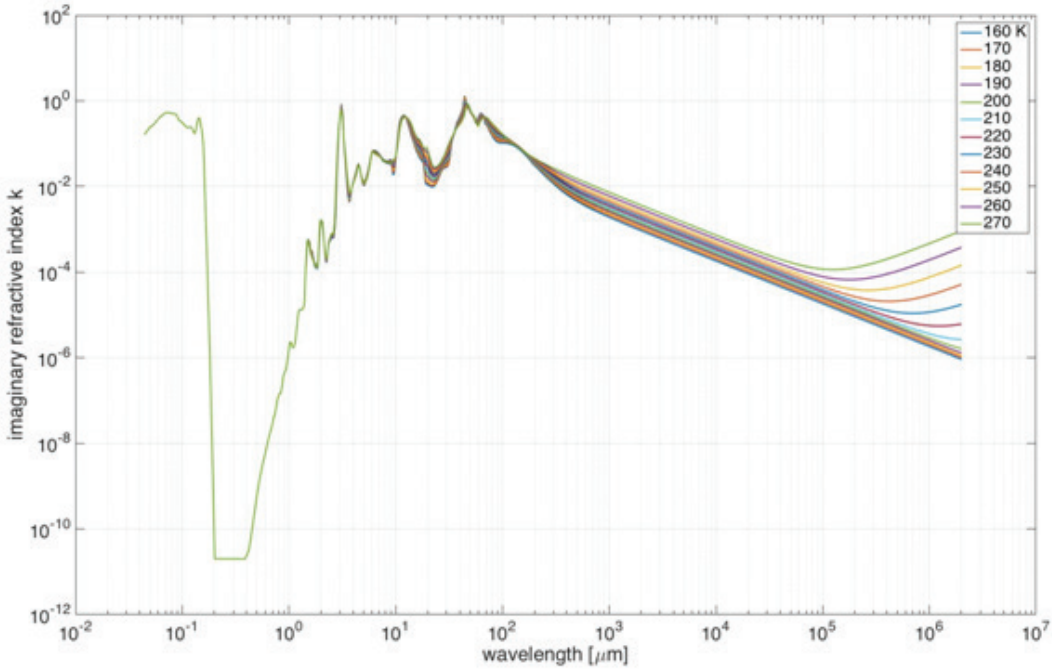

Figure 4. *Temperature dependence of the imaginary part of the index of refraction of water ice. Data from Iwabuchi and Yang (2011).*

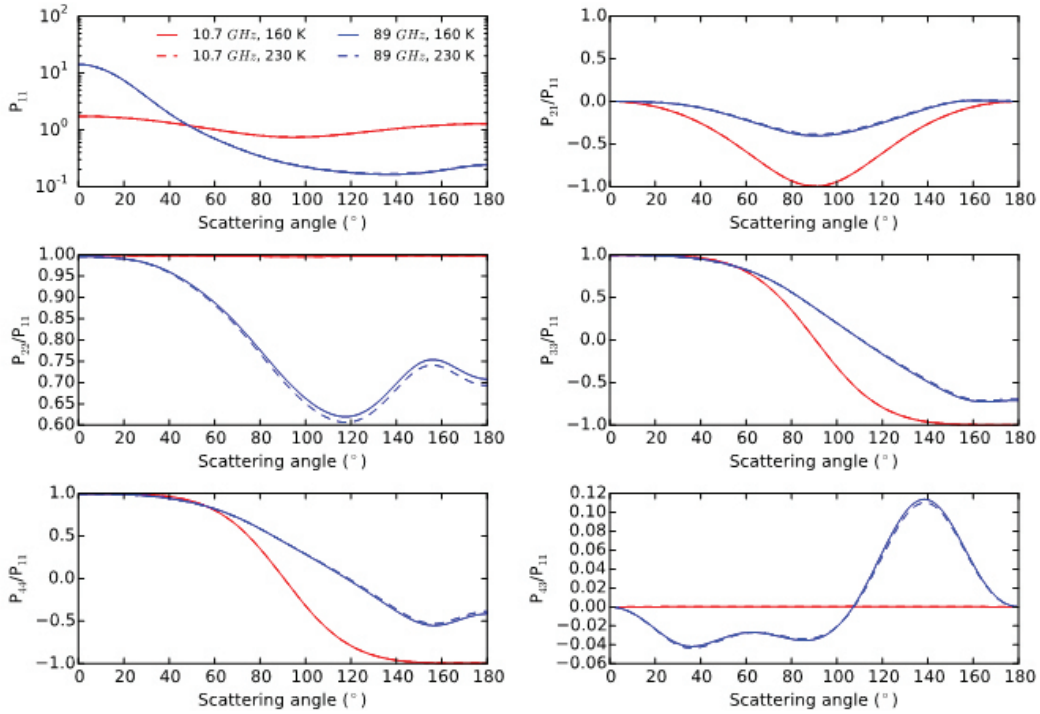

Figure 5. *Effect of the temperature dependence on the bulk phase matrix of MC6 ice cloud model for particles with an effective radius of 800 μm at frequencies of 10.7 and 89 GHz and at temperatures of 160 and 230 K. Adapted from Yi et al. (2016).*

Sounder (AIRS) infrared are shown in Fig. 6 (Yi et al., 2016). The bias of the default coefficients with respect to the observations does not occur with the MC6 single-scattering properties.

To allow for a variable mass density of graupel and snow particles as listed in Table 1 with a highly irregular and porous morphology, the Bicontinuous Random

(continued on page 11)

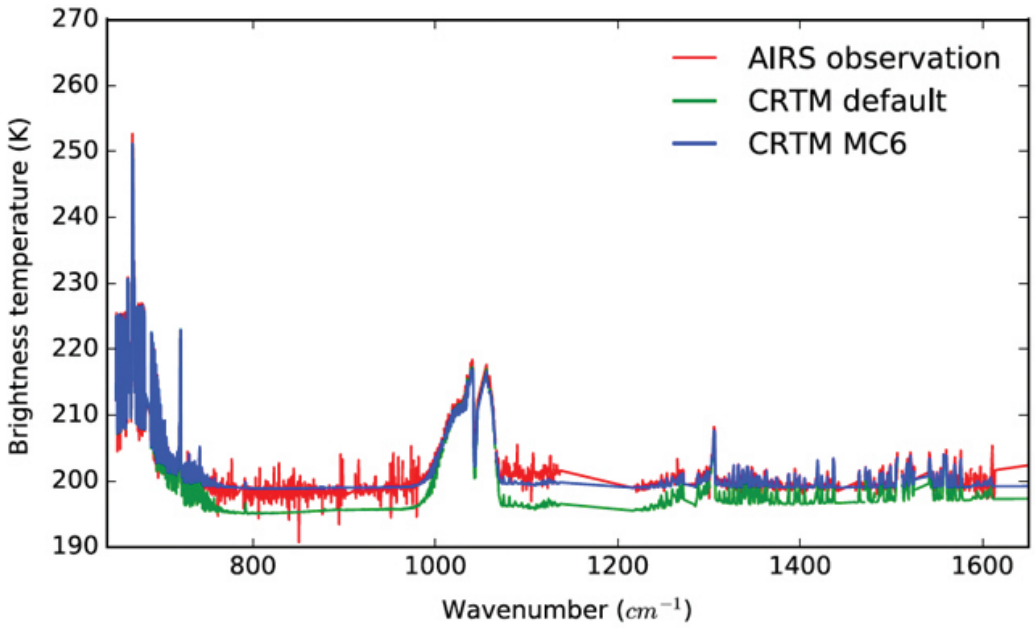

Figure 6. *Comparison between AIRS observations, CRTM default ice cloud scattering properties and MC6 scattering table data. Adapted from Yi et al. (2016).*

Figure 7. *BRM model of a conical graupel particle used for scattering calculations.*

Medium (BRM) model (Berk, 1991) has been proposed. The application of this morphological model to graupel has been discussed by Tang et al. (2017) and Stegmann et al. (2018). In the graupel case, it was found (Tang et al., 2017) that the density and granularity of the particle has a more significant effect on the MW scattering properties than the prediction from a simple effective medium model. The case of snow further allowed opportunities to study the effect of vastly different aspect ratios. It was found (Stegmann et al., 2018) that plate-like aspect ratios reduce the influence of the density on the phase function, but have no effect on other properties, such as the extinction coefficient and the single-scattering albedo. An illustration of the BRM concept and the produced highly irregular morphology in the case of a conical graupel particle are shown in Fig. 7.

Furthermore, we have developed an ice crystal single-scattering property database in the microwave spectral region (1 to 874 GHz) to provide the scattering, absorption, and polarization properties of 12 ice crystal habits (10-plate aggregate, 5-plate aggregate, 8-column aggregate, solid hexagonal column, hollow hexagonal column, hexagonal plate, solid bullet rosette, hollow bullet rosette, droxtal, oblate spheroid, prolate spheroid, and sphere) with particle maximum dimensions from 2 μm to 10 mm (Ding et al., 2017). For each habit, four temperatures (160, 200, 230, and 270 K) are selected to account for temperature dependence of the ice refractive index. The microphysical and scattering properties include projected area, volume, extinction efficiency, single-

(continued on page 12)

scattering albedo, asymmetry factor, and six independent nonzero phase matrix elements (i.e. P_{11}, P_{12}, P_{22}, P_{33}, P_{43} and P_{44}). To illustrate the application of the aforesaid database, we computed the IWC-Z_e relations (shown in Fig. 8) for three single-habit ice particle models and one habits mixture model at temperatures 200 and 230 K based on 1117 PSDs obtained from a dataset of *in situ* measurements in several field campaigns. Least-square fitting is applied to each computed IWC-Z_e distribution to get the best-fit linear regressions as written and plotted in Fig. 8. It can be seen that the red and blue dots in each subplot in Fig. 8 nearly overlap. This suggests that temperature has little effect on equivalent radar reflectivity at 94 GHz, which is a common frequency of cloud radar. While the PSD naturally depends on temperature, in active microwave remote sensing of ice clouds, the temperature dependence of ice particle single-scattering properties is not significant.

Summary

Our Texas A&M group has been working with the CRTM team to improve the accuracy in considering the scattering effect associated with hydrometeors. State-of-the-art scattering computational capabilities in terms of a synergistic combination of the invariant-imbedding T-matrix method and the improved geometric optics method have been used to compute the single-scattering properties that have been incorporated into the CRTM. Specifically, the ice cloud single-scattering properties of the CRTM have been revised using the MC6 optical properties. The change of the refractive

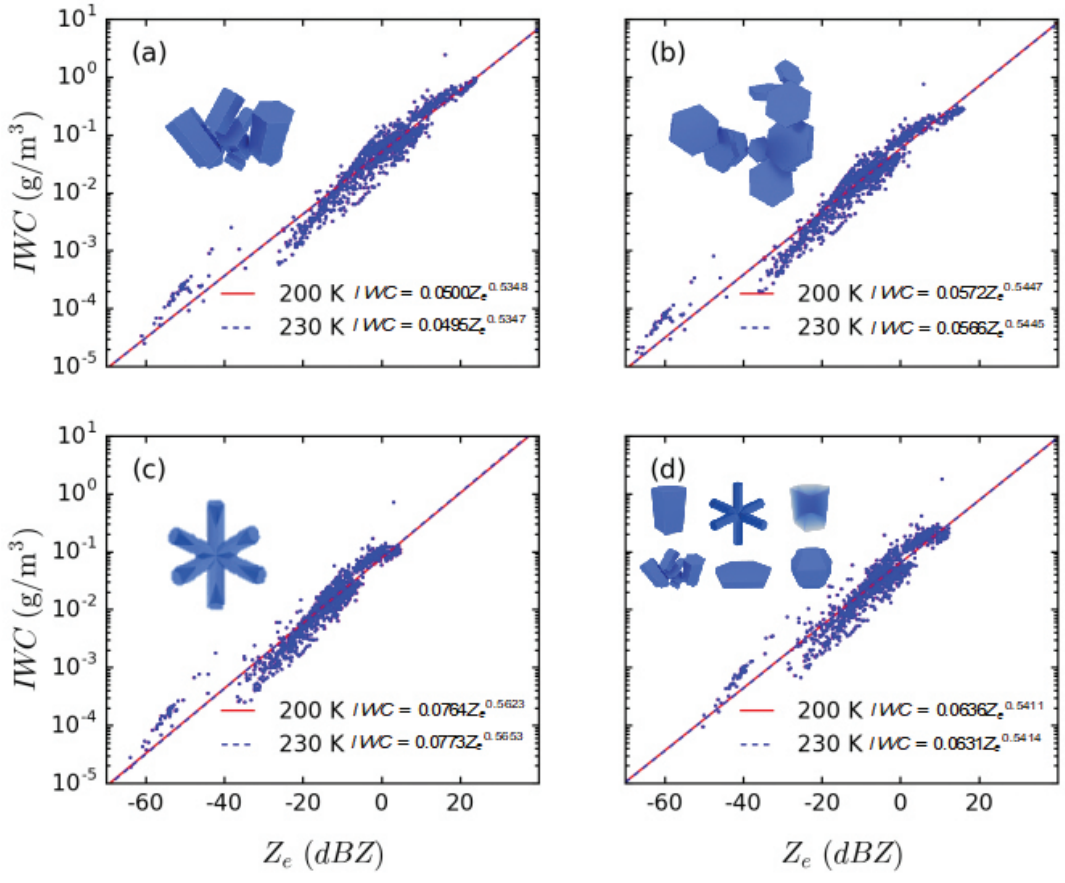

Figure 8. *Z_e-IWC relations at 94 GHz computed using three single-habit models and one habit mixture model at temperatures 200 and 230 K. Colors represent temperature. Dots are calculated Z_e-IWC relations values from individual measurements. Solid and dashed lines are the least-square fitted Z_e-IWC relations. (a): 8-column aggregate; (b): 10-plate aggregate; (c): hollow bullet rosette; (d): habits mixture. Adapted from Ding et al. (2017).*

(continued on page 13)

index is accounted for based on the data of Iwabuchi and Yang (2011) and the variation of the particle density for graupel and snow classes of the CRTM has been enabled through the application of the Bicontinuous Random Medium approach.

Ping Yang, Patrick G. Stegmann, Guanglin Tang, Souichiro Hioki and Jiachen Ding, Department of Atmospheric Sciences, Texas A&M University, 3150 TAMU, 77840 College Station, TX, USA pyang@tamu.edu*; Benjamin T. Johnson, NOAA Center for Weather and Climate Prediction, 5830 University Research Ct. 20740 College Park, MD, USA*

Acknowledgements

This project was supported by NOAA Grant NA15NES4400003 and partly by the endowment funds related to the David Bullock Harris Chair in Geosciences at the College of Geosciences, Texas A&M University. A major portion of the calculations was carried out at the Texas A&M University Supercomputing Facilities, and the authors gratefully acknowledge the facility staff for their help and assistance.

References

Baum, B. A., P. Yang, A. J. Heymsfield, S. Platnick, M. D. King, Y. X. Hu, and S. M. Bedka, 2005: Bulk Scattering Properties for the Remote Sensing of Ice Clouds. II: Narrowband Models. *J. Appl. Meteor.* 44, 1896-1911.

Berk, N. F., 1991: Scattering properties of the leveled-wave model of random morphologies. *Physical Review A* 44, pp. 5069-5079.

Bi, L., and P. Yang, 2014: Accurate simulation of the optical properties of atmospheric ice crystals with invariant imbedding T-matrix method. *J. Quant. Spectrosc. Radiat. Transfer*, 138, 17-35.

Ding, J., L. Bi, P. Yang, G. W. Kattawar, F. Weng, Q. Liu, and T. Greenwald, 2017: Single-scattering properties of ice particles in the microwave regime: temperature effect on the ice refractive index with implications in remote sensing, *J. Quant. Spectrosc. Radiat. Transfer*, 190, 26-27.

Heidinger, A. K., C. O'Dell, R. Bennartz, and T. Greenwald, 2006: The Successive-Order-of-Interaction Radiative Transfer Model. Part I: Model Development. *J. Appl. Meteor. and Clim*. 45, pp. 1388-1402.

Iwabuchi, H., and P. Yang, 2011: Temperature dependence of ice optical constants: Implications for simulating the single-scattering properties of cold ice clouds. *J. Quant. Spectrosc. Radiat. Transfer,* 112, 2520-2525.

Liu, Q., and F. Weng, 2006: Advanced Doubling-Adding Method for Radiative Transfer in Planetary Atmospheres. *J. Atmo. Sci.* 63, 3459-3465.

McCumber, M., W.-K. Tao, and J. Simpson, 1991: Comparison of Ice-Phase Microphysical Parameterization Schemes Using Numerical Simulations of Tropical Convection. *J. Appl. Meteor.* 30, 985-1004.

Platnick, S., K. G. Meyer, M. D. King, G. Wind, N. Amarasinghe, B. Marchant, G. T. Arnold, Z. Zhang, P. A. Hubanks, R. E. Holz, P. Yang, W. L. Ridgway, and J. Riedi, 2017: The MODIS Cloud Optical and Microphysical Products: Collection 6 Updates and Examples from

(continued on page 14)

Terra and Aqua. *IEEE Trans Geosci. Remote Sensing* 55, 502-524.

Stegmann, P. G., G. Tang, P. Yang, B. T. Johnson, 2018: A Stochastic Model for Density-Dependent Microwave Sow- and Graupel Scattering Coefficients of the NOAA JCSDA Community Radiative Transfer Model. *J. Quant. Spectrosc. Radiat. Transfer,* 211, 9-24.

Tang, G., P. Yang, P. G. Stegmann, R. L. Panetta, L. Tsang, and B. Johnson, 2017: Effect of particle shape, density, and inhomogeneity on the microwave optical properties of graupel and hailstones. *IEEE Trans Geosci. Remote Sensing*, 55, 6366-6378.

Yang, P., and K. N. Liou, 1996a: Geometric-Optics-integral-equation method for light scattering by nonspherical ice crystals, *Appl. Opt*., 35, 6568-6584

Yang, P., and K. N. Liou, 1996b: Finite-difference time domain method for light scattering by small ice crystals in three-dimensional space. *J. Opt. Soc. Am A* 13, 2072-2085.

Yee, S. K., 1966: Numerical solution of initial boundary value problems involving Maxwell's equations in isotropic media. *IEEE Trans Antennas Propag*. 14, 302–7.

Yi, B., P. Yang, Q. Liu, P. van Delst, S.-A. Boukabara, and F. Weng, 2016: Improvements on the ice cloud modeling capabilities of the Community Radiative Transfer Model. *J. Geophys Res*. 121. doi:10.1002/2016JD025207

Sub-daily variation in observations, satellite retrievals, and model simulations of aerosol optical depth

Introduction

Aerosol prediction is a mission-critical requirement for applications requiring forecasts of visibility and air quality. Forecast models at higher resolutions can potentially resolve finer features in both space and time, including variation within the day which can be especially important in coastal environments and near surface pollution sources. However, global model resolutions are still coarse relative to many of the phenomena that drive sub-daily variation, and the model atmosphere is smoother than the real atmosphere even at fully resolved scales.

Development of aerosol data assimilation systems, as well as satellite verification of model forecasts, was driven mainly by products from polar-orbiting sensors especially the Moderate Resolution Imaging Spectroradiometer (MODIS) on the NASA Terra and Aqua satellites. Advanced sensors on recently launched geostationary satellites offer capability for

(continued on page 15)

retrieval of aerosol over a broader portion of the diurnal cycle. Geostationary Aerosol Optical Depth (AOD) products suitable for operational assimilation are expected to become available in the near future. It is therefore timely to examine the nature and extent of sub-daily variation in aerosols, the capability of satellite observations and model analyses to capture this variation, and the potential for improving aerosol predictions by assimilation of geostationary AOD data.

Data and Simulations

AERONET from KORUS-AQ

The Korean-US Air Quality study (KORUS-AQ), a joint mission led by the Korean National Institute of Environmental Research and the US National Aeronautics and Space Administration (NASA), included an intensive field measurement campaign lasting roughly six weeks in May - June 2016 (https://www-air.larc.nasa.gov/missions/korus-aq/). During this period, several dozen sun photometer instruments were deployed by NASA's Aerosol Robotic Network (AERONET; [*Holben et al.*, 1998]). We use these data (Version 3 Level 2.0 aerosol product) to examine the relative magnitude of daily and subdaily variation in AOD. The uncertainty of AOD retrieved by AERONET direct sun measurements is on the order of +/-0.015 [*Schmid et al.*, 1999], which is sufficient for our purposes to use these data as truth for comparison with satellite-based retrievals and model simulations.

GOCI Level 2 aerosol retrieval

The Geostationary Ocean Color Imager (GOCI) on board the Korean Communication, Ocean and Meteorological Satellite 1 (COMS-1) is a high-resolution multispectral imager with 8 bands at 500 m resolution between 412 and 865nm. GOCI takes imagery over a domain covering Korea, Japan, and eastern China eight times a day, hourly from 00Z to 07Z. The Yonsei Aerosol Retrieval (YAER) Version 2 [*Choi et al.*, 2018] is a look-up table (LUT) retrieval using a minimum reflectivity technique to constrain surface reflectance, and incorporating specific tests for cloud and turbid water. Aerosol Optical Depth, Ångström Exponent, Fine-mode Fraction, and Aerosol Single Scattering Albedo are retrieved at 6 km spatial resolution from each GOCI scene. For visualization and comparison with AERONET, GOCI retrievals were screened using the built-in product QA to select only retrievals where all aerosol properties were successfully retrieved. For this study, a research product combining the YAER V2 AOD algorithm with additional cloud screening based on infrared observations from the Himawari-8 Advanced Himawari Imager (AHI) was used. For data assimilation, additional screening was performed (see below).

NAAPS model

The Navy Aerosol Analysis and Prediction System (NAAPS) is a modeling system developed at the Naval Research Laboratory that simulates sources, sinks, and transport of four aerosol species (anthropogenic/biogenic fine-mode particles, dust, smoke, and sea salt), as well as gaseous sulfur dioxide. The model configuration is described in detail in Lynch et al. [2016]. The configuration used for these experiments mostly matches Lynch et al. [2016], with these important differences:

- NAAPS was run for KORUS-AQ at the current operational resolution of 1/3 degree;

(continued on page 16)

- NAAPS output was generated every 3 hours;
- We evaluate two identically configured NAAPS runs, one initialized by assimilation of MODIS AOD only (labeled KORUS_2633) and the other using MODIS and GOCI AOD (labeled KORUS_2G33).

Level 3 AOD products for assimilation in NAAPS

The NAAPS model forecast is initialized by assimilation of satellite AOD using a 3-D variational (actually 2-D since AOD is a uniformly weighted column integral) method as described by Zhang et al. [2008]. Two AOD datasets are assimilated in this study. The first is MODIS AOD, based on Collection 6 Dark Target [*Levy et al.*, 2013] and Deep Blue [*Sayer et al.*, 2013] retrievals, with additional processing to reduce noise and remove biases as described by Shi et al. [2011] and Hyer et al. [2011]. The second product assimilated is the Yonsei University GOCI+AHI retrieval as described above. GOCI retrievals were screened by a "buddy check" as well as a local variance check, rejecting retrievals with no adjacent retrievals as well as retrievals more than +/- 0.3 standard deviations (Z-score) from the 3x3 local mean AOD. All satellite retrievals were aggregated to an 0.5-degree grid with a +/-1.5 hour time window around the analysis time prior to assimilation, rejecting grid cells with fewer than 5 MODIS or 30 GOCI retrievals.

Selection of a paired sample (AERONET+ GOCI Level 2) for analysis

The 24-hour cycle is intrinsically undersampled by both sun photometry and satellite retrievals, as both depend on sunlit, cloud-free conditions for retrieval of AOD. Studies with very limited nighttime AOD data (e.g. Perez-Ramirez et al. [2016]) indicate that trends and variability in column aerosol properties during nighttime are similar to daytime. Satellite retrievals have additional limitations, due to problems with retrievals when the sun is low to the horizon. Model data are available for all locations and times in the domain.

To obtain a fully paired dataset for analysis, the GOCI+AHI retrievals were sampled to select the valid GOCI+AHI retrieval nearest to each valid AERONET retrieval. When no valid GOCI+AHI retrieval is available within +/-30 minutes and +/-25 km, the data point is excluded from the paired sample. This method resulted in 19,195 measurements from 42 AERONET stations over 43 days of the KORUS-AQ mission, 1 May – 18 June 2016. Note that this sample is geographically limited to the GOCI domain (see Figure 3).

Subdaily variation was estimated by calculating the mean AOD from all valid retrievals for each AERONET site for each date. These site/day means were then subtracted from the full datasets to obtain "subdaily anomalies" of AOD. This procedure was repeated for the AERONET, satellite, and model datasets.

Estimates of sub-daily variation will be suppressed by partial obscuration of the data, such as by cloudy conditions. Days with partially cloudy conditions are likely to have less sub-daily variation in the observations, an artifact of observation limitations. To obtain an estimate based on more complete observations of daytime variation, we examined each AERONET

(continued on page 17)

site for each day, and selected sites/days with valid AERONET retrievals within +/- 30 minutes of 0900, 1200, and 1500 local solar time. This "clear-day subset" resulted in 179 sites/days with relatively complete sampling of the diurnal cycle for analysis.

Results

Variance in daily means and subdaily anomalies at AERONET sites

Figure 1 shows the total variance in the paired datasets from AERONET, GOCI, and the NAAPS analyses. Also shown is the partitioning of the total variance into daily means and subdaily anomalies. Results are shown for both the "clear-day subset" and the complete set of data paired to AERONET.

Satellite and model skill at capturing AERONET observed variance

To compare the satellite and model AOD datasets to AERONET, we used the entire set of AERONET data for the KORUS-AQ domain and time period, rather than the

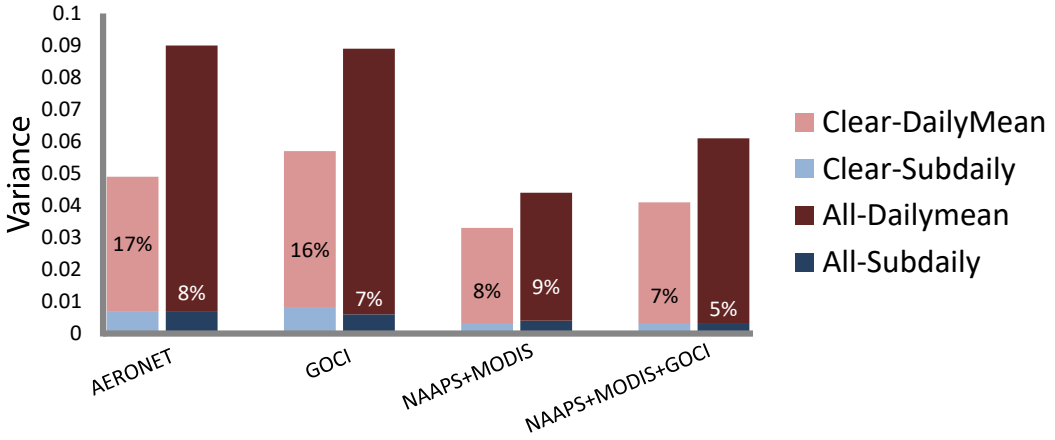

Figure 1. *AOD variance divided into daily-mean and subdaily-anomaly components for AERONET, satellite, and model AOD datasets. Numbers indicate the fraction of total variance not captured by the daily mean.*

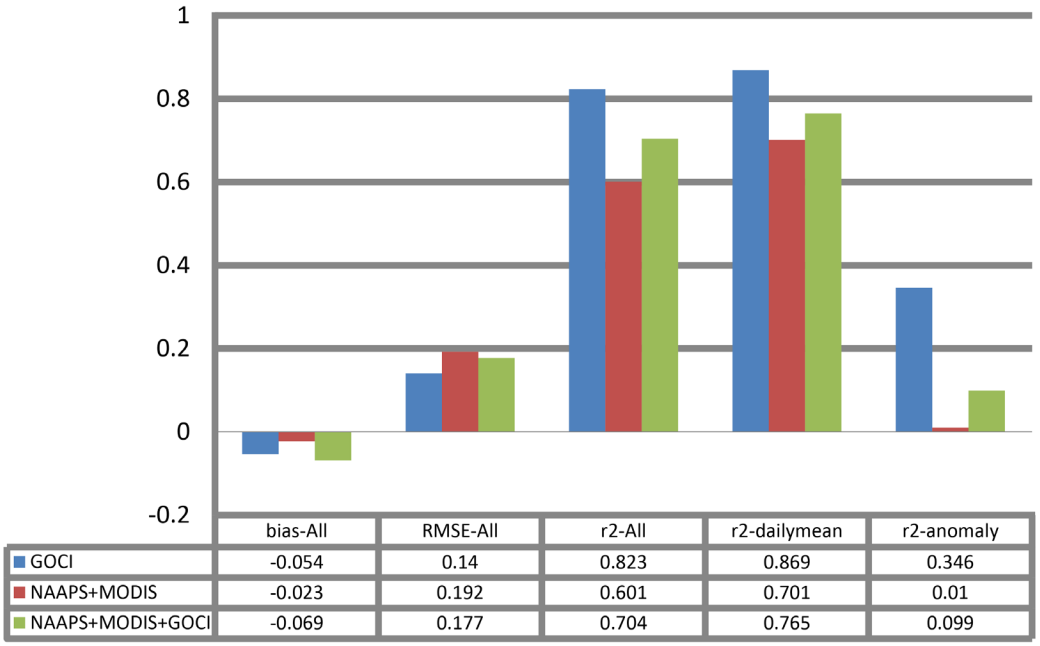

	bias-All	RMSE-All	r2-All	r2-dailymean	r2-anomaly
GOCI	-0.054	0.14	0.823	0.869	0.346
NAAPS+MODIS	-0.023	0.192	0.601	0.701	0.01
NAAPS+MODIS+GOCI	-0.069	0.177	0.704	0.765	0.099

Figure 2. *Comparison of satellite retrieved AOD and NAAPS model analysis to AERONET during KORUS-AQ.*

(continued on page 18)

very limited "clear-day subset." Figure 2 shows the bias, root-mean-squared error, and correlation coefficient R2 for satellite and model AOD vs AERONET, and also the R2 values indicating the skill of the satellite and model datasets at capturing the variance in the AERONET daily mean and subdaily anomaly. For these comparisons, day/site mean values and subdaily anomalies were calculated separately for each dataset.

Satellite AOD variance across the GOCI domain

Figure 3 shows the mean AOD, days with valid observations, and mean observations per day (excluding days with 0 observations) for the Yonsei V2 GOCI+AHI AOD product. The variance analysis was extended to the complete GOCI+AHI dataset, by taking the time variance for each pixel over the 344 GOCI scenes (8x/day * 43 days) and dividing into daily-mean and subdaily-anomaly components. Figure 4 shows the total variance, variance of the subdaily anomaly, and ratio of the subdaily anomaly variance to the total variance, for each pixel in the GOCI domain for the study period.

Discussion

The mean AOD (Figure 3A) highlights the densely industrialized areas of eastern China, Korea, and Japan, demonstrating the predominance of anthropogenic aerosol in this domain during the KORUS-AQ time period. AOD variance over land generally matches the patterns of large anthropogenic surface sources. A notable exception can be seen in the upper right of the maps, especially over Hokkaido, where the limited number of successfully retrieved days resulted in a

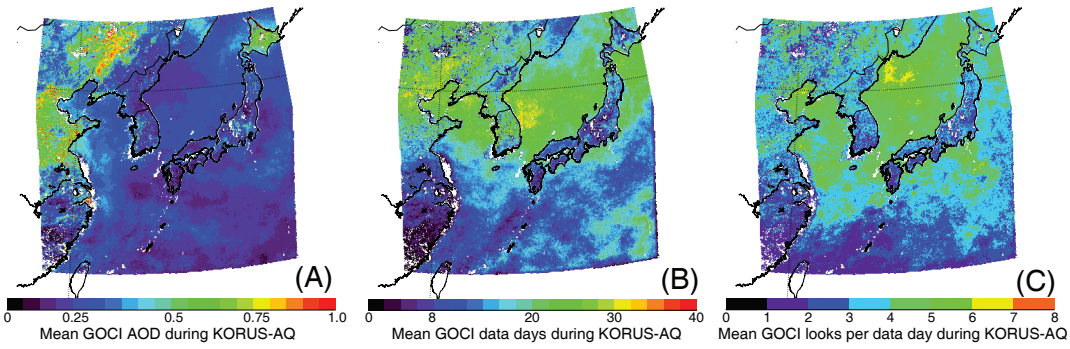

Figure 3. *Retrievals from Yonsei University Version 2 GOCI+AHI AOD retrieval. (A) Mean AOD during KORUS-AQ. (B) Number of days with valid retrievals during KORUS-AQ (out of maximum 43). (C) Mean number of valid AOD retrievals per day with >0 data (maximum of 8/day).*

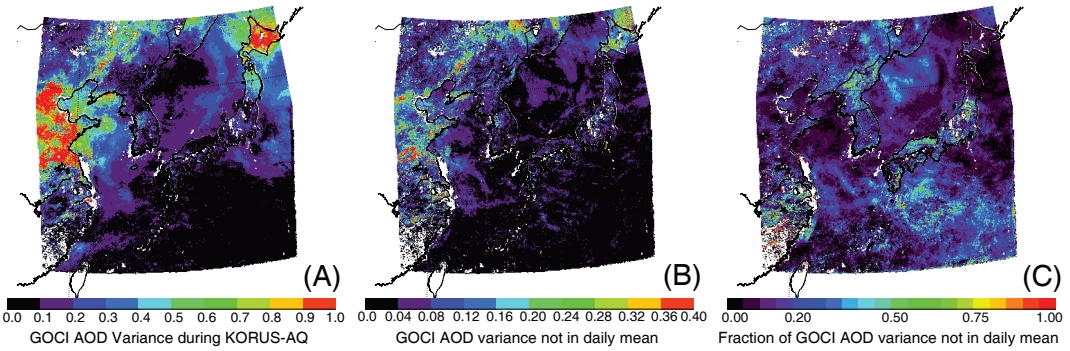

Figure 4. *Temporal variance of GOCI AOD during KORUS-AQ as a function of location. (A) Total variance, (B) variance of subdaily anomaly (note different scale), (C) fraction of total variance not captured by daily mean.*

(continued on page 19)

time series dominated by several long-range transport events (See AERONET plot for Hokkaido University), leading to elevated mean AOD and variance during KORUS-AQ.

Figure 5 shows time series and scatter plots comparing NAAPS analysis with assimilation of MODIS (KORUS_2633) and MODIS+GOCI (KORUS_2G33) to AERONET measurements from Hokkaido University. The NAAPS model analysis matches observations well, but the inclusion of GOCI AOD in the Naval Research Laboratory (NRL) Atmospheric Variational Data Assimilation System for AOD (NAVDAS-AOD) led to significantly improved representation in the time series, especially capturing the low AOD observed immediately before and after the high-AOD

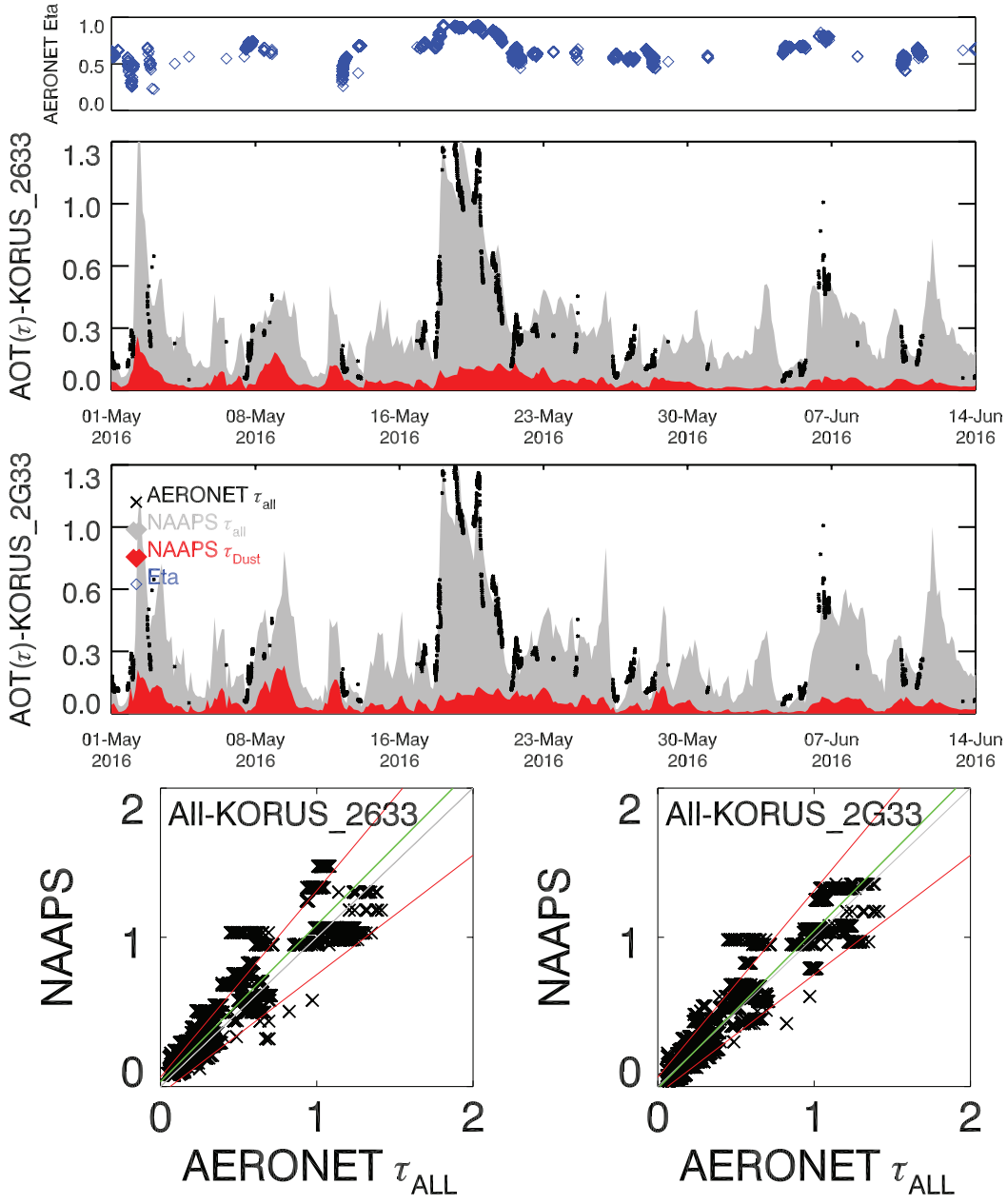

*Figure 5. Comparison of NAAPS analyzed AOD using MODIS (KORUS_2633) and MODIS+GOCI(KORUS_2G33) versus AERONET sun photometer data from Hokkaido University. The top plot shows the contribution of fine-mode aerosol to AERONET AOD. The middle two plots show time series comparing AERONET to the two different NAAPS analyses: the AERONET AOD is shown as black dots, the grey contour is NAAPS total AOD, and the red contour is NAAPS AOD from the dust tracer. The bottom scatter plots compare AERONET (X axis) to NAAPS analysis sampled to match the AERONET data (Y axis), with the ordinary least-squares best-fit line shown in green and the error tolerances corresponding to AOD(NAAPS)=AOD_AERONET+/-(0.05+0.2*AOD_AERONET).*

(continued on page 20)

events on 17-22 May. The addition of GOCI AOD reduces the NAAPS root-mean-square errors (RMSE) for this station by 25% (from 0.135 to 0.106), and eliminates a positive bias in the NAAPS-MODIS run (bias reduced from +0.051 to +0.007).

Over the broad domain, the bias of NAAPS-MODIS is close to 0 (see Figure 2), so the negative bias of the GOCI data results in a negative bias in NAAPS-MODIS+GOCI. The verification results for the Yonsei V2 GOCI AOD retrieval [*Choi et al*., 2018], based on comparison of five years of AERONET and GOCI retrieved AOD (March 2011 to February 2016, so not including the KORUS-AQ time period), do not indicate this negative bias. However, several possible causes must be considered, though additional studies would be required to quantify these effects:

- Calibration drift of GOCI: Figure 8c of Choi et al. [2018] indicates a change in annual mean bias from positive bias in 2011 to negative bias in 2015.
- Climatological surface reflectance database: the Yonsei V2 algorithm uses data from March 2011 to February 2016 to estimate surface reflectance, these estimates may be biased relative to later dates.
- Additional screening: Using the AHI infrared channels to stringently filter potentially cloudy pixels will inevitably result in removal of some high aerosol events in addition to cloud-contaminated retrievals [*Hyer et al*., 2011], which could cause an additional low bias.
- Persistence of afternoon observations: The analysis of Choi et al. does show a small diurnal cycle, with a slight positive bias at midday and negative bias in the morning and evening retrievals. Because the evening retrievals are followed by a period with no data available for assimilation, it could be that the negative bias of these evening retrievals persists resulting in an overall negative bias that is larger for the NAAPS-MODIS+GOCI analysis than for the GOCI data by themselves.

The daily means for each site capture more than 80% of the variance in the AERONET data even for the "clear-day" subset (Figure 1). GOCI AOD shows a similar breakdown of variance, with subdaily variance accounting for as much as 60% of overall variance in some areas with low total variance, but generally less than 20% (Figure 4C). However, the subdaily anomalies in the GOCI data are only weakly correlated to the AERONET anomalies (Figure 2). This indicates that diurnal variation in GOCI AOD may be very noisy at the 6km retrieval scale. The systematic diurnal variation in AOD bias versus AERONET noted by Choi et al. is small, but may be a significant contributor to subdaily variance with no equivalent signal in AERONET data.

Both the GOCI data and the NAAPS model show good skill at capturing the variance in daily means observed by AERONET (Figure 2). The satellite data perform better than the NAAPS-MODIS analysis (R^2=0.87 vs R^2=0.70), and the NAAPS-MODIS+GOCI analysis bridges the difference but is still out-performed by the raw satellite retrievals.

The total variance of AOD from the NAAPS model is very low compared to either AERONET or GOCI. The variance of the

(continued on page 21)

subdaily anomaly is also smaller for NAAPS, but because of the lower total variance, the fraction of variance in the subdaily anomaly is similar. Assimilation of MODIS+GOCI increases the NAAPS variance significantly, but the increased variance is largely in the daily mean rather than the subdaily anomaly. This is another consequence of the persistence of AOD information from the analysis: the impact of GOCI data in reducing the area with no observations on each day is more important than the variation imparted from the GOCI data to the analysis over multiple assimilation cycles on the same day.

Conclusions

The clear statistical improvement in NAAPS analysis makes a strong case for assimilation of geostationary AOD data, but the absence of sub-daily variation in the NAAPS model output may be a limitation of scale. The NAAPS nominal spatial resolution of 1/3 degree should be adequate to capture many sub-daily phenomena, especially those that are transport-related, but the NAVDAS-AOD assimilation scheme uses a fixed second-order autoregressive (SOAR) scheme to spatially spread information from observations [*Zhang et al*., 2008], which results in significant smoothing at scales of multiple NAAPS grid cells. It is highly likely that a more advanced data assimilation scheme including flow-dependent error correlations (e.g. Rubin et al. [2017]) will lead to significantly better resolution of subdaily variation in the atmospheric aerosol.

Edward J. Hyer (Marine Meteorology Division, Naval Research Laboratory, Monterey CA), edward.hyer@nrlmry.navy.mil
David A. Peterson (Marine Meteorology Division, Naval Research Laboratory, Monterey CA)
Peng Xian (Marine Meteorology Division, Naval Research Laboratory, Monterey CA)
Jianglong Zhang (Department of Atmospheric Science, University of North Dakota, Grand Forks ND)
Myungje Choi (Yonsei University, Seoul, Korea)
Mijin Kim (Yonsei University, Seoul, Korea)
Jhoon Kim (Yonsei University, Seoul, Korea)

Note: The analysis in this article was presented in January 2018 at the American Meteorological Society Annual Meeting: https://ams.confex.com/ams/98Annual/meetingapp.cgi/Paper/325605

Acknowledgements

This research was supported by the Office of Naval Research Code 322. KORUS-AQ data analysis was supported by NASA grant #NNH16AC52i "Advanced Geostationary and Lidar Data Exploration." The authors wish to thank the AERONET PIs especially the Hokkaido University site PIs Dr. Brent Holben (NASA GSFC) and Dr. Teppei Yasunari (Hokkaido University).

References

Choi, M., J. Kim, J. Lee, M. Kim, Y. J. Park, B. Holben, T. F. Eck, Z. Q. Li, and C. H. Song (2018), GOCI Yonsei aerosol retrieval version 2 products: an improved algorithm and error analysis with uncertainty estimation from 5-year validation over East Asia, *Atmospheric Measurement Techniques, 11*(1), 385-408, doi:10.5194/amt-11-385-2018.

Holben, B. N., et al. (1998), AERONET - A federated instrument network and data archive for aerosol characterization, *Remote Sens. Environ., 66*(1), 1-16.

Hyer, E. J., J. S. Reid, and J. Zhang (2011), An over-land aerosol optical depth data set for

(continued on page 22)

data assimilation by filtering, correction, and aggregation of MODIS Collection 5 optical depth retrievals, *Atmospheric Measurement Techniques, 4*(3), 379-408, doi:10.5194/amt-4-379-2011.

Levy, R. C., S. Mattoo, L. A. Munchak, L. A. Remer, A. M. Sayer, F. Patadia, and N. C. Hsu (2013), The Collection 6 MODIS aerosol products over land and ocean, *Atmospheric Measurement Techniques, 6*(11), 2989-3034, doi:10.5194/amt-6-2989-2013.

Lynch, P., et al. (2016), An 11-year global gridded aerosol optical thickness reanalysis (v1.0) for atmospheric and climate sciences, *Geoscientific Model Development, 9*(4), 1489-1522, doi:10.5194/gmd-9-1489-2016.

Perez-Ramirez, D., H. Lyamani, A. Smirnov, N. T. O'Neill, I. Veselovskii, D. N. Whiteman, F. J. Olmo, and L. Alados-Arboledas (2016), Statistical study of day and night hourly patterns of columnar aerosol properties using sun and star photometry, in *Remote Sensing of Clouds and the Atmosphere Xxi*, edited by A. Comeron, E. I. Kassianov, K. Schafer, J. W. Jack, R. H. Picard and K. Weber, Spie-Int Soc Optical Engineering, Bellingham, doi:10.1117/12.2242372.

Rubin, J. I., J. S. Reid, J. A. Hansen, J. L. Anderson, B. N. Holben, P. Xian, D. L. Westphal, and J. L. Zhang (2017), Assimilation of AERONET and MODIS AOT observations using variational and ensemble data assimilation methods and its impact on aerosol forecasting skill, *J. Geophys. Res.-Atmos., 122*(9), 4967-4992, doi:10.1002/2016jd026067.

Sayer, A. M., N. C. Hsu, C. Bettenhausen, and M. J. Jeong (2013), Validation and uncertainty estimates for MODIS Collection 6 "Deep Blue" aerosol data, *J. Geophys. Res.-Atmos., 118*(14), 7864-7872, doi:10.1002/jgrd.50600.

Schmid, B., J. Michalsky, R. Halthore, M. Beauharnois, L. Harrison, J. Livingston, P. Russell, B. Holben, T. Eck, and A. Smirnov (1999), Comparison of aerosol optical depth from four solar radiometers during the Fall 1997 ARM Intensive Observation Period, *Geophys. Res. Lett., 26*(17), 2725-2728.

Shi, Y., J. Zhang, J. S. Reid, B. Holben, E. J. Hyer, and C. Curtis (2011), An analysis of the collection 5 MODIS over-ocean aerosol optical depth product for its implication in aerosol assimilation, *Atmos. Chem. Phys., 11*(2), 557-565, doi:10.5194/acp-11-557-2011.

Zhang, J. L., J. S. Reid, D. L. Westphal, N. L. Baker, and E. J. Hyer (2008), A system for operational aerosol optical depth data assimilation over global oceans, *J. Geophys. Res.-Atmos., 113*(D10), 13, doi:10.1029/2007jd009065.

EDITOR'S NOTE

I hope you take time to read the strong trio of science contributions featured in this edition of the JCSDA Quarterly Newsletter. Ping Yang and co-authors have documented improvements in microwave interactions with various forms of frozen precipitation particles as an advancement to the CRTM. (We'll be welcoming one of those co-authors, Patrick Stegmann, to join us in College Park, MD, later this month as a core member of the CRTM Project.) Ed Hyer of NRL and his co-authors have provided a case indicating the potential value of using geosynchronous-based aerosol optical depth (AOD) retrievals in operational analyses, though noting the challenges that arise from the lack of sub-daily variation within their modeling system. And A. R. Naeger et al have contributed an article discussing how to use multi-sensor AODs measurements to improve radiance assimilations for NWP.

I confess to feeling a measure of relief - and a great deal of satisfaction - that so many of the events I wrote of looking forward to in this space a few months ago have come to pass. Most dramatically, JCSDA Director, Tom Auligne, and I had the good fortune to be at Kennedy Space Center on Cape Canaveral, FL, to witness the successful launch of the GOES-S (now GOES-17) satellite. My formal role there was to speak with members of the press and the public regarding the exploitation of GOES-17 observations along with other satellite data to improve numerical weather prediction forecasting and situational awareness of weather and environmental hazards to help government agencies, industries, and individuals make the best decisions based on these observations and our value-added science. As the team that built and launched GOES-17 began their well-deserved celebration, I thought that for others of us, the real work is just beginning.

Therefore, it's equally gratifying (if not so flashy) to report that the JCSDA Executive Team and Project Leads had a very productive retreat at Estes Park, CO, early in February. Over the span of 2½ days, we were able to complete a first draft of the Annual Operating Plan for the period from April 1, 2018–March 31, 2019. Final details and adjustments to the plan are being made, but the Management Oversight Board has received the draft plan favorably. This puts us on a firm footing for continuing and expanding our work over the next year.

It also sets the stage for the 16th Annual JCSDA Science Review and Technical Meeting, which will be held at NOAA's David Skaggs Research Center in Boulder, CO, May 30–June 1, 2018. Please be on the look-out for email circulars about the Annual Meeting and look for links on the JCSDA Webpage to register and access additional information as the Meeting approaches. The Annual Meeting provides an opportunity not only to review what has been accomplished during the past year and how that work will be carried forward, but also to explore new directions and to ensure that efforts by all of the JCSDA partners are as complementary and coordinated as possible. We look forward to seeing you there!

Jim

SCIENCE CALENDAR

UPCOMING EVENTS

MEETINGS AND EVENTS SPONSORED BY JCSDA

DATE	LOCATION	TITLE
May 30-31, June 1, 2018	Boulder, CO	JCSDA Annual Science Workshop
July 22-August 3, 2018	Bozeman, MT	JCSDA Annual Summer Colloquium 2018

MEETINGS OF INTEREST

DATE	LOCATION	WEBSITE	TITLE
May 7–10, 2018	Montreal, Canada	http://web.meteo.mcgill.ca/enkf/	8th EnKF Workshop Montreal
June 26–28, 2018	Lisbon, Portugal	http://cimss.ssec.wisc.edu/iswg/meetings/2018/	2nd International surface working group (ISWG)
July 1–6, 2018	Aveiro, Portugal	http://www.morgan.edu/research_and_economic_development/gestar_adjoint_workshop/first_announcement.html	11th Workshop on Meteorological Sensitivity Analysis and Data Assimilation
December 10–14, 2018	Washington, D.C., USA	https://fallmeeting.agu.org/	AGU fall meeting

CAREER OPPORTUNITIES

Opportunities in support of JCSDA may also be found at http://www.jcsda.noaa.gov/careers.php as they become available.